Revisiting Structural and Electromechanical Properties of the Lead-free (K,Na)NbO 3 High-Piezoelectric Material

Laurent Bellaiche, Yali Yang, Charles Paillard

Revisiting Structural and Electromechanical Properties of the Lead-free (K,Na)NbO_3 High-piezoelectric Material

Laurent Bellaiche,[1,2,*] Yali Yang,[3,*] and Charles Paillard[1,4]

[1]*Smart Ferroic Materials Center, Physics Department and Institute for Nanoscience and Engineering, University of Arkansas, Fayetteville, Arkansas 72701, USA*

[2]*Department of Materials Science and Engineering, Tel Aviv University, Ramat Aviv, Tel Aviv 6997801, Israel*

[3]*School of Mathematics and Physics, University of Science and Technology Beijing, Beijing 100083, China and*

[4]*Laboratoire Structures, Propriétés et Modélisation des Solides, CentraleSupélec, UMR CNRS 8580, Université Paris-Saclay, 91190 Gif-sur-Yvette, France*

Abstract

Having lead-free systems with excellent piezoelectric response is crucial to the development of environmentally-friendly electromechanical applications. In this work, we build an effective Hamiltonian model to explore the promising (K_xNa_{1-x})NbO_3 system, whose rich phase diagram near $x = 50$ % remains poorly understood meanwhile exhibiting a colossal effective piezoelectric response. Thanks to the numerical implementation of this effective Hamiltonian scheme into a Monte-Carlo Metropolis algorithm, we reveal striking features. Firstly, a long-period state can be the ground state at low temperatures for some concentrations while only a short-period, conventional polar ground state exists for larger x. Secondly, the electric-field-driven transformation, via a first-order transition, of this long-period state into a short-period polar state creates large electromechanical strains (on the order of the percent) and is likely the origin of the colossal piezoelectric response reported in KNN, for which we evaluate an effective piezoelectric coefficient of several thousands of pC/N.

KEYWORDS: (K,Na)NbO_3, High piezoelectricity, Effective Hamiltonian, Phase transition, Nanotwin states

I. INTRODUCTION

Piezoelectric materials, which convert an electrical signal into a mechanical deformation and vice versa, are indispensable components in modern technologies[1–3]. Due to growing environmental and health concerns about the traditional lead-based piezoelectric materials [e.g., $Pb(Zr,Ti)O_3$ (PZT) and $Pb(Mg,Nb,Ti)O_3$ (PMN-PT)], the pursuit of environmentally friendly alternatives to lead-based materials has intensified in recent years. Potassium-sodium niobate $(K_xNa_{1-x})NbO_3$ (KNN) is one of their most prominent representatives for applications such as actuators, sensors, and energy harvesting devices[3–5].

Particularly, KNN with compositions x near 50% are intriguing, as many phases with distinct polarization directions and octahedra tilting patterns have been suggested for this compositional region, leading to rich and complex tentative phase diagrams[6–9]. In addition, giant piezoelectricity has been reported in these complex lead-free systems[4,10,11]. Yet, the origin of the exceptional piezoelectric properties and associated large electrically-induced strain in KNN systems remains unclear. Some have attributed the large piezoelectric response to the existence of a low-symmetry, morphotropic phase boundary (MPB) phase in-between high-symmetry ones[3], similar to systems such as PZT or PMN-PT[12–14]. Others in Ref. [4] have suggested that multidomains exist in some compositional range of KNN, and the electric-field-induced transformation from the multidomain state to the monodomain state results in a giant strain (0.92%) and a colossal effective piezoelectric coefficient $d^*_{33} \approx 9,000$ pm/V. Giving the interest as well as complexity and richness of the physical phenomena involved, it is timely to resolve the microscopic origin of the giant electromechanical response in KNN by advanced computational methods capable of revealing the electrical, mechanical and structural properties of KNN at finite temperature and electric fields.

In this work, we develop an atomistic effective Hamiltonian (H_{eff}) for KNN systems with compositions close to 50% and reveal the existence of long-period states being ground states for some potassium concentration which then become metastable in favor of a short-period ground state for larger K compositions. Finite electric-field simulations strongly suggest that the transformation of this long-period phase into a short-period phase is the origin of the large electromechanical strain reported by Hu *et al.*[4].

II. METHODS

The effective Hamiltonian method essentially maps the complex energy landscape in KNN based on a reduced number of important degrees of freedom: (1) the local soft mode $\boldsymbol{u}_i$, which is proportional to the electric dipole of the 5-atom cell i and which we technically center on the A-sites of the ABO_3 perovskite structure[15,16]; (2) the homogenous strain tensor, $\{\eta_H\}$; (3) the $\boldsymbol{v}_j$ dimensionless variables that are related to the inhomogeneous strains within the 5-atom cell j[15,16] and that we chose to center on Nb sites; (4) the pseudo-vector $\boldsymbol{\omega}_j$ that characterize the oxygen octahedral tiltings[17] (also named antiferrodistortive (AFD) distortions) in the 5-atom unit cell j, and that are also centered on Nb sites; and (5) the $\{\sigma_i\}$ variables that determine the atomic configuration of the solid solutions, since σ_i=+1 or -1 is chosen here to indicate the presence of a K or Na ion, respectively, at the A-lattice site i. The total energy can then be expressed as:

$$E_{tot}(\{\boldsymbol{u}_i\},\{\eta_H\},\{\boldsymbol{v}_j\},\{\boldsymbol{\omega}_j\},\{\sigma_i\}) = E_{VCA}(\{\boldsymbol{u}_i\},\{\eta_H\},\{\boldsymbol{v}_j\},\{\boldsymbol{\omega}_j\}) + E_{alloy}((\{\boldsymbol{u}_i\},\{\boldsymbol{v}_j\},\{\boldsymbol{\omega}_j\},\{\sigma_i\}) \quad (1)$$

where E_{VCA} is the effective Hamiltonian energy of a virtual simple system, <K-Nb>NbO_3, for which the A-cation <K-Nb> represents an average of 50% of K and 50% of Nb ions, following the so-called virtual crystal approximation (see Ref. [18] and references therein). The analytical expression of E_{VCA} is precisely that used in Ref. [19].

The E_{alloy} energy gathers corrections needed to realistically model the real $(K_xNa_{1-x})NbO_3$ solid solutions with respect to its VCA approximation. Its proposed expression is:

$$E_{alloy}((\{\boldsymbol{u}_i\},\{\boldsymbol{v}_j\},\{\boldsymbol{\omega}_j\},\{\sigma_i\}) = \sum_i \{\Delta\kappa_2(\sigma_i)u_i^2 + \Delta\alpha(\sigma_i)u_i^4 + \Delta\gamma(\sigma_i)(u_{i,x}^2u_{i,y}^2 + u_{i,y}^2u_{i,z}^2 + u_{i,z}^2u_{i,x}^2)\} \quad (2)$$

$$+ \sum_{i,k} Q_{k,i}(\sigma_k)\mathbf{e}_{ki}\cdot\mathbf{u}_i$$

$$+ \sum_{m,l} R_{l,m}(\sigma_l)\mathbf{f}_{lm}\cdot\mathbf{v}_m$$

$$+ \Delta\kappa_A \sum_{m.l} \sigma_l\ \omega_m^2$$

where the first sum runs over all the A-sites i, and where $\Delta\kappa_2(\sigma_i)$, $\Delta\alpha(\sigma_i)$ and $\Delta\gamma(\sigma_i)$ are coefficients that are "only" σ-dependent and that characterize the effect of alloying on

on-site contributions for the local modes. The second sum also runs over all the A-sites i, as well as their six first-nearest neighbors (within the A-sublattice) k, with $\mathbf{e}_{ki}$ being the unit vector along the direction joining the A-center k to the A-center i. The third and fourth sum rather run over all the Nb-sites m and their eight first-nearest neighbors (within the A-sublattice) l, with $\mathbf{f}_{lm}$ being the unit vector along the direction connecting the A-center l to the Nb-center m. Practically, the second and third terms represent the effect of alloying on intersites interactions with the local modes and inhomogeneous strains, respectively. They can be thought as representing the effect of local electric field and local strain fields (due to alloying), respectively, on properties of KNN. The last line characterizes how alloying locally affects the oxygen octahedral tiltings, which is important in KNN. This latter term incorporates the facts that pure $KNbO_3$ does not want such tiltings to occur while these structural deformations are essential features of pure $NaNbO_3$[9,20].

All the parameters involved in Eqs (1) and (2), including $Q_{k,i}(\sigma_k)$, $R_{l,m}$ and $\Delta\kappa_A$, are provided in the Supporting Information and are determined by performing first-principle calculations on small cells (typically, up to 40 atoms) using the local density approximation (LDA)[21,22] within density functional theory and the virtual crystal approximation[18]. Practically, the CUSP code is employed[18] that takes advantage of the ultrasoft-pseudopotential scheme[23]. Our pseudopotentials include the following valence electrons[24]: $3s^2 3p^6 4s^1$ for K, $2s^2 2p^6 3s^1$ for Na, $4s^2 4p^6 4d^4 5s^1$ for Nb and $2s^2 2p^4$ for O ions. A 25 Ry plane-wave cutoff is chosen along with a $6 \times 6 \times 6$ mesh for a 5-atom cell. The extracted values of the parameters are given in Tables S1 and S2 of the Supporting Information.

This H_{eff} is then implemented in Metropolis Monte Carlo (MC) algorithms, enabling to simulate the finite-temperature and electric-field properties of KNN in a $12 \times 12 \times 12$ supercell (corresponding to 8,640 atoms). *Disordered* solid solutions with different compositions are simulated by randomly selecting the $\{\sigma_i\}$ variables within the A-sublattice and keeping them frozen during the computations. Some outputs of these MC simulations are: (1) the supercell average of the local mode vectors, denoted $< \mathbf{u_\Gamma} >$, which is proportional to the electric polarization; (2) the $< \omega_\mathbf{R} >$ pseudovector, that quantifies antiphase tilting of the oxygen octahedra[17] and that is equal to $\omega_\mathbf{R} = \frac{1}{N}\sum_i \omega_i (-1)^{n_x(i)+n_y(i)+n_z(i)}$, where the sum runs over all the Nb sites i and where $n_x(i)$, $n_y(i)$ and $n_z(i)$ are integers denoting the lattice position of cell i (this cell i is centered at $a_{lat}(n_x(i)\mathbf{x} + n_y(i)\mathbf{y} + n_z(i)\mathbf{z})$, with a_{lat} being the 5-atom cubic lattice constant); and (3) the homogeneous strain tensor $< \eta_H >$, with its six

components in Voigt notation[25]. Note that the x-, y- and z-axes in the entire manuscript correspond to the pseudocubic [100], [010] and [001] directions, respectively.

III. RESULTS AND DISCUSSION

Let us first investigate properties of $(K_xNa_{1-x})NbO_3$ with $x = 0.50$ (coined KNN-50) as a function of temperature. For that we chose a disordered alloy configuration with 50% of K and 50% of Na ions within the A-sublattice of the ABO_3 perovskite structure, and cool down such system from 500K to 10K, using 40,000 MC sweeps at each temperature. The resulting $< \mathbf{u_\Gamma} >$, $< \omega_\mathbf{R} >$ and $\{\eta_H\}$ are shown in Figs 1a, 1b and 1c, respectively, when averaging these physical quantities over the last 20,000 MC sweeps for each temperature (the first 20,000 MC sweeps are used to reach thermodynamic equilibrium). These three panels indicate that the presently developed H_{eff} predicts that above $\simeq$ 430K, KNN-50 adopts the paraelectric cubic $Pm\bar{3}m$ structure – as evidenced by $< \mathbf{u_\Gamma} >=\mathbf{0}$, $< \omega_\mathbf{R} >=\mathbf{0}$, $< \eta_{H,4} >=< \eta_{H,5} >=< \eta_{H,6} >=0$ while $< \eta_{H,1} >=< \eta_{H,2} >=< \eta_{H,3} >$ have identical non-zero values (note that the zero of strain corresponds to the LDA-predicted lattice constant of KNN-50 in its cubic paraelectric state at 0K). Then, a first-order transition towards the ferroelectric tetragonal P4mm state occurs at $\simeq$ 430K, with the z-component of $< \mathbf{u_\Gamma} >$ becoming finite (characterizing a polarization lying along [001]) and $< \eta_{H,3} >$ suddenly increasing while $< \eta_{H,1} >=< \eta_{H,2} >$ experiences a sharp decrease. On the other hand, $< \omega_\mathbf{R} >$ remains null, which indicates that the oxygen octahedral tiltings are still not long-range ordered despite the fact that these AFD distortions are locally significant since $< |\omega_\mathbf{R}| >$ is close to 0.118 radians, that is about 6.8°, at 420K. KNN-50 remains within this P4mm phase when further cooling down to $\simeq$ 320K; temperature at which the ferroelectric orthorhombic Amm2 phase occurs via another first-order transition. This latter phase transition is characterized by (i) the y-component of $< \mathbf{u_\Gamma} >$ taking a finite value and becoming equal to its z-component, the polarization now aligning with the [011] direction; (ii) $< \eta_{H,2} >$ jumping to reach the positive value of $< \eta_{H,3} >$, while $< \eta_{H,1} >$ becomes even more negative; and (iii) the shear strain, $< \eta_{H,4} >$, adopting a finite value while $< \eta_{H,5} >=< \eta_{H,6} >$ remain null. This Amm2 phase persists under cooling until $\simeq$ 270K, before transforming, via a third first-order transition, into a ferroelectric rhombohedral R3m state for which the electrical polarization lies along [111] – as evidenced by $< u_{\Gamma,x} >=< u_{\Gamma,y} >=< u_{\Gamma,z} >\neq 0$ (see Fig. 1a) and

all the diagonal elements of the homogeneous strain tensor being finite and equal to each other, as the shear elements of $\{\eta_H\}$ do too (cf. Fig 1c). The supercell average of the antiphase oxygen octahedral tilting still vanishes, as indicated by the fact that $<\omega_{\mathbf{R}}>=\mathbf{0}$ and as consistent with the R3m space group. On the other hand, these tiltings do adopt a long-range order below $\simeq$ 80K, therefore making the R3m state continuously evolving into a R3c rhombohedral state inside which a polarization along [111] now coexists with oxygen octahedra tilting in antiphase about this [111] direction (see $<\omega_{R,x}>=<\omega_{R,y}>=<\omega_{R,z}>$ being finite below 80K in Fig 1b). In fact,this coexistence originates from the fact that the local AFD motions collaboratively couple with electric local dipoles because of a specific term in the E_{VCA} energy of Eq. (1)[19] – namely the term involving E_{xyxy} in Equation (S4) of the Supporting Information.

Remarkably, all these $Pm\bar{3}m$, P4mm, Amm2, R3m and R3c states have been reported in pure or pure slightly-doped $(K_xNa_{1-x})NbO_3$ compounds with x close to 50%[8,9,26–29], therefore confirming the qualitative power of the H_{eff} methods to describe complex materials[14–17,19,30–34]. Note also that the first-order nature of the $Pm\bar{3}m$-P4mm and P4mm-Amm2 transitions has indeed been found in KNN (see, e.g., Ref.[26]) while that of Amm2-R3m has been observed in some other perovskites (see, e.g., Ref. [35]). Similarly, the second-order character of the R3m-R3c transition has been reported in some perovskite compounds[36,37]. Quantitatively, the experimental $Pm\bar{3}m$-P4mm critical temperature of about 673 K[8,26,27] is underestimated, as typical for the H_{eff} methods[15,16] (probably due to the fact that all the parameters of these effective Hamiltonians are determined at 0K, which may cause inaccuracy for large transition temperatures). On the other hand, the predicted P4mm-Amm2 transition temperatures of $\simeq$ 320K is closer to the experimental values of 473 K[8,27]. In particular, both experiments and our simulations found the orthorhombic Amm2 phase to be the equilibrium state at room temperature. It is also interesting to notice that Ref. [8] reported that Amm2 transforms into a phase called X in KNN-50 at around $\simeq$250K-265K, which is rather close to our predicted temperature of 270K at which our R3m state appears. Moreover, Ref. [8] also indicated the appearance of a R3c state (from this X phase) at temperatures of 160K-190K, which is of the same order than our 80K prediction for the presently predicted R3m-R3c transition temperature.

Let us now concentrate on disordered $(K_xNa_{1-x})NbO_3$ with $x = 0.43$, to be denoted as KNN-43, adopting the same procedure as KNN-50. Results of the MC simulations are

depicted in Figs 1d, 1e and 1f. In that case, the first-order $Pm\bar{3}m$-P4mm transition is predicted to happen at $\simeq$ 430K, which is similar to that of KNN-50 and which is thus consistent with the observation that such transition is rather insensitive to composition in KNN for a large range of compositions[9]. At around 310K and as similar to the case of KNN-50, P4mm transforms via a first-order transition too into an Amm2 phase with polarization along [011] (see Fig 1d)– also in agreement with reports that the P4mm-Amm2 transition is rather insensitive to K compositions over a wide window of concentrations[9]. Within this ferroelectric orthorhombic Amm2 phase, the positive $< \eta_{H,2} >=< \eta_{H,3} >$ and $< \eta_{H,4} >$, as well as the negative $< \eta_{H,1} >$ are mostly independent of the temperature, similarly to the Amm2 state of KNN-50 (see Fig. 1c). Then, $< \eta_{H,1} >$ becomes less negative and $< \eta_{H,2} >=< \eta_{H,3} >$ decreases as the temperature is reduced below 270K in KNN-43, which is in sharp contrast with what is happening in the Amm2 phase of KNN-50 and KNN-43. As we will see later, these features are an indication that this state in KNN-43 is not anymore the Amm2 phase for temperatures ranging between $\simeq$ 180K and $\simeq$ 270K. For now, we will refer to it as the Y phase. Note that conducting Fourier transforms of the local dipolar pattern helps in confirming the structural difference between Amm2 and the Y-phase. Remarkably, Figs 1d-1f further reveal that neither R3m nor R3c state happens in KNN-43 under further cooling. One rather sees a new phase emerging below $\simeq$ 170K for which antiphase oxygen octahedra adopt a long-range order, tilting nearly about the [011] direction – with the polarization continuing to mostly lie along the [011] direction. This new phase is coined here the Z-phase.

Let us now investigate this Z-phase in more details and compare some of its properties with those of the R3c state, at 10K and as a function of composition. We will limit ourself to a range of K composition x varying between 40% and 60% since the employed H_{eff} can be considered (by construction) to a be perturbation of the one for KNN-50 and therefore compositions deviating too much from 50% may not be well modeled. It is worthwhile to know that we numerically found that both the Z-phase and R3c are stable states within this 40-60% compositional range at 10K. Their difference in energy is drawn in Fig 2a, which reveals that the Z-phase is of lower energy than R3c for K compositions below $\simeq$ 47% while R3c is the ground-state for compositions above it, as consistent with the low-temperature results of Figs 1 for KNN-50 and KNN-43. When concentrating on KNN-43, we numerically found that it is the last term of Eq. (2) that makes the energy of the Z-phase to become

lower than that of R3c, while the first three sums of that Equation only weakly modify the properties of KNN. In other words, it is the fact that local oxygen octahedra surrounded by K prefer to tilt much less than those with Na ions in KNN that destabilizes the R3c state in favor of the Z-phase. In contrast, the VCA system and its perturbations involving local modes and inhomogeneous strains (that are the first three terms of Eq. (2)) would prefer the R3c state to be the ground state. In fact, these first three terms have only slight effects on properties of KNN as demonstrated by the fact that the $< u_{\Gamma,x} >=< u_{\Gamma,y} >=< u_{\Gamma,z} >$ of R3c and the $< u_{\Gamma,y} >=< u_{\Gamma,z} >$ of the Z-phase only very slightly change with composition between 40% and 60% (see Fig. 2b and its small vertical scale). On the other hand, the importance of the last term of Eq. (2) is further manifested in the strong decrease of $< \omega_{R,y} >=< \omega_{R,z} >$ in the Z-phase and of $< \omega_{R,x} >=< \omega_{R,y} >=< \omega_{R,z} >$ in the R3c state as the K concentration increases from 40 to 60%. Such decrease also explains why the ground state of KNN with K compositions above $\simeq$ 60% is experimentally known to be R3m rather than R3c[9], that is the long-range anti-phase oxygen octahedral tilting is annihilated for these latter concentrations.

Figure 2c shows the microstructure of this Z-phase. At a fist glance, it can be thought as 71° domains for the local dipoles, for which domains having a local polarization along the $[\bar{1}11]$ direction alternate along the $[0\bar{1}1]$ direction with domains for which the local polarization lies along the [111] direction; with the antiphase oxygen octahedral tiltings reacting to these polar domains by adopting their own domains: one type for which the axis of the oxygen octahedra tilting is parallel or antiparallel to $[\bar{1}11]$ and the other type having such oxygen octahedral axis being parallel or antiparallel to [111][39,40]. However, the line profiles along the $[0\bar{1}1]$ direction of the local modes and oxygen octahedral tiltings reported in Figs 2e and f reveal that the Z-phase is not really a multidomain state but rather a state for which the x-components of the electric dipoles and of the ω_i pseudo-vectors oscillate and adopt a long-period. As such, the Z-phase can be classified as one example of the nanotwin states that have been discussed in Refs. [31,41] and that have been found in several systems, including $BiFeO_3$ under pressure[42], rare-earth-doped $BiFeO_3$[43–45] or Li-doped $NaNbO_3$[46]. The occurence of these nanotwin phases originates from the trilinear coupling associated with the first energetic term of the last line of Eq. (S4) of the Supporting Information. Note that such latter energy is enhanced as the K composition decreases since the oxygen octahedral titlings become larger, as shown in Fig. 2c. Note also that we numerically found

that changing some conditions, such as the size of the supercell or some starting data, may affect the specific characteristics of the Z-phase (such as its long-range period) but this Z-phase always remains a nanotwin state (as consistent with the fact that several nanotwin states can have very similar energy). It is also worthwhile to realize that the maxima of the local modes in Fig. 2e does not coincide with those of the oxygen octahedral tiltings of Fig. 2f, implying that one may also see the Z-state as a real-space separation between phases where local electric dipoles are large and phases for which AFD motions are significant.

We also numerically found that the dipolar pattern of the Y-phase is rather similar to that of the Z-phase, that is it exhibits a long-period for the x-components of the electric dipoles along the $[0\bar{1}1]$ direction. On the other hand, the organized patterns made by the oxygen octahedral tiltings vanish in favor of more disordered AFD motions, as consistent with the fact that $< \omega_{\mathbf{R}} >= \mathbf{0}$ in the Y-phase – as indicated in Fig. 1e. Note, however, that tiltings of oxygen octahedra still occurs locally in the Y-phase, as indicated by the large value of $< |\omega_{\mathbf{R}}| >$ depicted in Fig. 1e between 170K and 270K. These significant local AFD motions still couple with electric local dipoles because of the last line of Equation (S4) of the Supporting Information. Note also that Ref. [4] experimentally found domains in KNN-43 at room temperature, but interpreted them as 180° domains with electric dipoles being parallel to the $< 100 >$ pseudo-cubic direction alternating with domains having electric dipoles being along the opposite $< \bar{1}00 >$ direction. Due to the fact that KNN with K compositions close to 50% is known to have electric dipoles having x, y and z-components at room temperature[47–49], it is likely that the phase seen in Ref. [4] have also y- and/or z-components, in addition to x-components, for its electric dipoles, which will make it resembling our Y-phase. We thus invite experimentalists to confirm our hypothesis.

Let us now attempt to explain the large electromechanical responses reported in KNN near room temperature for some narrow range compositions but not for others[4]. For that, we will concentrate on KNN-43 and compare the piezoelectric response of two stable phases both at 260 K, that is the (short-period) R3m state and the (long-period) Y-domain-phase. Our R3m phase has an electrical polarization lying along the [111] direction and we apply an electric field about the x-direction and up to a (small) value of 5×10^7 V/M. Figure 3a indicates that the application of such fields simply slightly increases the x-component of the polarization while its y- and z-components are slightly reduced. The R3m phase is thus transformed into a monoclinic Cm (still of short-period) phase having a polarization along

$[vuu]$ directions ($v > u$). Because of the coupling between electric dipoles and strains, such behaviors result in the *change* of $< \eta_{H,1} >$ (with respect to its zero-field value) to nearly linearly increase with the field, reaching a value of $\simeq 0.19\%$ for our highest field (see Fig. 3b). We extract an effective piezoelectric coefficient of 360 $\pm$30 pC/N, which agrees with the reported values ranging between $\simeq$ 100 and 600 pC/N in pure or doped KNN with x close to 50%[4,50,51].

Regarding the Y-phase at 260K, we also apply an electric field along the x-direction, that is the direction for which $< u_{\Gamma,x} > \simeq 0$ as a result of the oscillation of the x-components of the electric dipoles. In that case, Figure 3a shows that increasing such field from zero to 0.2×10^7 V/m weakly increases the x-component of the polarization while the y- and z-components barely change. Therefore, the complex structure of the Y-phase is essentially insensitive to such weak fields. Then for a field of about 0.21-0.22 $\times$ 10^7 V/m, a first-order transition occurs towards the aforementioned short-period monoclinic Cm phase having a polarization along $[vuu]$. Subsequently, and exactly as for the initial R3m-phase, further increase of the electric field then makes the x-component of the polarization slightly strengthening while the y- and z-components are weakly reduced. Remarkably, the first-order transition is accompanied by a huge change of $< \eta_{H,1} >$ of about 0.64% with respect to the zero-field value (see Fig 3b). This remarkable change of strain is fully consistent with the reported 0.96% strain[4] for a field of similar magnitude. The associated effective piezoelectric coefficient is $\simeq$ 3,000 pC/N, consistent with the electromechanical response of multidomain KNN[4]. The small discrepancy in strain changes and field magnitude between our present simulations and experiments[4] may come from structural defects in the samples, unlike in our simulations, which favor the nucleation of the monoclinic phase at smaller fields. Another explanation may be that our calculations are performed at 260 K (to remain in the Y-phase, see Fig. 1d) while experiments were conducted near 300 K and that results may be quite sensitive to temperature. For instance, for the smaller temperature of 220K, the electric field needed for the Y-phase-to-Cm transition to occur is higher (about 0.52×10^7 V/m) and the change of strain is smaller (about 0.50%), leading to a smaller effective piezoelectric coefficient of $\simeq$ 962 pC/N. Nonetheless, we reveal that large strains induced by relatively small electric fields in KNN-43 and close compositions originate from the existence of a long-period state under no field followed by a field-induced transition to a short-period monoclinic state. Note also that Ref. [4] believed that the monodomain obtained under a field applied along $< 100 >$

in KNN-43 has a polarization along $< 100 >$ while our simulations rather indicate that it is along $[vuu]$. It is also worthwhile to indicate that we numerically found that, starting with the Amm2 phase but at 280K rather than 260K (since Amm2 and not the Y-phase is stable at 280K) with a polarization along [011] for KNN-43 and applying an electric field along [100] yields a transition at a field of 0.2 x 107 V/m. Such transition generates a phase for which the polarization is basically along the [110] pseudo-cubic direction, with the change in $< \eta_{H,1} >$ with respect to its initial zero-field value being also very large, namely 1.07%.

IV. CONCLUSIONS

In summary, we have developed and used an atomistic effective Hamiltonian to shed more light into the physical properties of the lead-free material $(K_xNa_{1-x})NbO_3$ with compositions x near 50%. Our simulations predict that, e.g., (1) when x=0.5 the structural phase of KNN-50 transforms following the sequence $Pm\bar{3}m \rightarrow P4mm \rightarrow Amm2 \rightarrow R3m \rightarrow R3c$, as the temperature reduces; (2) while when x=0.43 the phase transition sequence of KNN-43 becomes $Pm\bar{3}m \rightarrow P4mm \rightarrow Amm2 \rightarrow$ Y-phase $\rightarrow$ Z-phase, as the temperature reduces, where the Y- and Z-phases are predicted to be two long-period nanotwin states. Furthermore, we reveal that a first-order transition from the Y-phase to the Cm short-period state is responsible for the large change of strain and therefore the large effective piezoelectric coefficent in KNN-43 under small electric field, which successfully explains the large electromechanical responses being recently discovered in KNN[4] near room temperature for some narrow range compositions.

Acknowledgments

L.B. and C.P. thank the ARO Grant No. W911NF-21-1-0113 and the Vannevar Bush Faculty Fellowship (VBFF) Grant No. N00014-20-1-2834 from the Department of Defense. Y.Y. acknowledges the support by National Natural Science Foundation of China (grant no. 12304115), Fundamental Research Funds for the Central Universities (Grant No. FRF-TP-24-039A) and 2023 Fund for Fostering Young Scholars of the School of Mathematics and Physics, USTB (Grant No. FRF-BR-23-01B).

Supporting Information

The Supporting Information is available free of charge at ACS Applied Materials & Inter-

faces.

Additional experimental details, including equations of the effective Hamiltonian, and extracted parameters.

Email Address

laurent@uark.edu; ylyang@ustb.edu.cn

Notes

The authors declare no competing financial interest.

V. REFERENCES

[1] Guo, R.; Cross, L. E.; Park, S. E.; Noheda, B.; Cox, D. E.; Shirane, G. Origin of the high piezoelectric response in $PbZr_{1-x}Ti_xO_3$. *Phys. Rev. Lett.* **2000**, *84*, 5423–5426.

[2] Sekhar, M. C.; Veena, E.; Kumar, N. S.; Naidu, K. C. B.; Mallikarjuna, A.; Basha, D. B. A Review on Piezoelectric Materials and Their Applications. *Cryst. Res. Technol.* **2023**, *58*, 2200130.

[3] Saito, Y.; Takao, H.; Tani, T.; Nonoyama, T.; Takatori, K.; Homma, T.; Nagaya, T.; Nakamura, M. Lead-free piezoceramics. *Nature* **2004**, *432*(7013), 84-87.

[4] Hu, C.; Meng, X.; Zhang, M.-H.; Tian, H.; Daniels, J. E.; Tan, P.; Huang, F.; Li, L.; Wang, K.; Li, J.-F.; Lu, Q.; Cao, W.; Zhou, Z. Ultra-large electric field–induced strain in potassium sodium niobate crystals. *Sci. Adv.* **2020**, *6*(13), eaay5979.

[5] Wu, J.; Xiao, D.; Zhu, J. Potassium–sodium niobate lead-free piezoelectric materials: past, present, and future of phase boundaries. *Chem. Rev.* **2015**, *115*(7), 2559-2595.

[6] Yamada, H.; Matsuoka, T.; Kozuka, H.; Yamazaki, M.; Ohbayashi, K.; Ida, T. Crystal Structure and Phase Transition Behavior in $(K_{1-x}Na_x)NbO_3$-Based Lead-Free Piezoelectric Ceramic over a Wide Range of Temperatures. *J. Appl. Phys.* **2016**, *120*(21), 214102.

[7] Koruza, J.; Liu, H.; Höfling, M.; Zhang, M.-H.; Veber, P. $(K,Na)NbO_3$-Based Piezoelectric Single Crystals: Growth Methods, Properties, and Applications. *J. Mater. Res.* **2020**, *35*(8), 990-1016.

[8] Gomes, M. M.; Vilarinho, R.; Pinho, R.; Almeida, A.; Noudem, J. G.; Costa, M. E. V.; Vilarinho, P. M.; Moreira, J. A. Revisiting the Phase Sequence and Properties of $K_{0.5}Na_{0.5}NbO_3$ Ceramics Sintered by Different Processes. *Ceram. Int.* **2021**, *47*(6), 8308-8314.

[9] Baker, D. W.; Thomas, P. A.; Zhang, N.; Glazer, A. M. A Comprehensive Study of the Phase Diagram of $K_xNa_{1-x}NbO_3$. *Appl. Phys. Lett.* **2009**, *95*(9), 091903.

[10] Jiang, M.; Zhang, J.; Rao, G.; Li, D.; Randall, C. A.; Li, T.; Peng, B.; Li, L.; Gu, Z.; Liu, X.; Huang, H. Ultrahigh Piezoelectric Coefficient of a Lead-Free $K_{0.5}Na_{0.5}NbO_3$-Based Single Crystal Fabricated by a Simple Seed-Free Solid-State Growth Method. *J. Mater. Chem. C* **2019**, *7*(47), 14845-14854.

[11] Wu, B.; Wu, H.; Wu, J.; Xiao, D.; Zhu, J.; Pennycook, S. J. Giant Piezoelectricity and High Curie Temperature in Nanostructured Alkali Niobate Lead-Free Piezoceramics through Phase Coexistence. *J. Am. Chem. Soc.* **2016**, *138*(47), 15459-15464.

[12] Li, F.; Zhang, S.; Xu, Z.; Wei, X.; Luo, J.; Shrout, T. R. Composition and Phase Dependence of the Intrinsic and Extrinsic Piezoelectric Activity of Domain Engineered (1-x)$Pb(Mg_{\frac{1}{3}}Nb_{\frac{2}{3}})O_3$-x$PbTiO_3$ Crystals. *J. Appl. Phys.* **2010**, *108*(3), 034106.

[13] Jaffe, B.; Roth, R. S.; Marzullo, S. Piezoelectric Properties of Lead Zirconate-Lead Titanate Solid-Solution Ceramics. *J. Appl. Phys.* **1954**, *25*(6), 809-810.

[14] Bellaiche, L.; García, A.; Vanderbilt, D. Finite-Temperature Properties of $Pb(Zr_{1-x}Ti_x)O_3$ Alloys from First Principles. *Phys. Rev. Lett.* **2000**, *84*(23), 5427-5430.

[15] Zhong, W.; Vanderbilt, D.; Rabe, K. M. Phase Transitions in $BaTiO_3$ from First Principles. *Phys. Rev. Lett.* **1994**, *73*(13), 1861-1864.

[16] Zhong, W.; Vanderbilt, D.; Rabe, K. M. First-Principles Theory of Ferroelectric Phase Transitions for Perovskites: The Case of $BaTiO_3$. *Phys. Rev. B* **1995**, *52*(9), 6301-6312.

[17] Kornev, I. A.; Bellaiche, L.; Janolin, P.-E.; Dkhil, B.; Suard, E. Phase Diagram of $Pb(Zr,Ti)O_3$ Solid Solutions from First Principles. *Phys. Rev. Lett.* **2006**, *97*(15), 157601.

[18] Bellaiche, L.; Vanderbilt, D. Virtual crystal approximation revisited: Application to dielectric and piezoelectric properties of perovskites. *Phys. Rev. B* **2000**, *61*(12), 7877.

[19] Yang, Y.; Xu, B.; Xu, C.; Ren, W.; Bellaiche, L. Understanding and Revisiting the Most Complex Perovskite System via Atomistic Simulations. *Phys. Rev. B* **2018**, *97*(17), 174106.

[20] Petkov, V.; Kim, J.-W.; Shastri, S.; Gupta, S.; Priya, S. Geometrical Frustration and Piezoelectric Response in Oxide Ferroics. *Phys. Rev. Mater.* **2020**, *4*(1), 014405.

[21] Hohenberg, P.; Kohn, W. Inhomogeneous Electron Gas. *Phys. Rev.* **1964**, *136*(3B), B864-B871;

[22] Kohn, W.; Sham, L. J. Self-Consistent Equations Including Exchange and Correlation Effects. *Phys. Rev.* **1965**, *140*(4A), A1133–A1138.

[23] Vanderbilt, D. Soft Self-Consistent Pseudopotentials in a Generalized Eigenvalue Formalism. *Phys. Rev. B* **1990**, *41*(11), 7892.

[24] King-Smith, R. D.; Vanderbilt, D. First-Principles Investigation of Ferroelectricity in Perovskite Compounds. *Phys. Rev. B* **1994**, *49*(9), 5828–5844.

[25] Nye, J. F. *Physical Properties of Crystals, Their Representation by Tensors and Matrices*; Clarendon Press: Oxford, 1957.

[26] Ishizawa, N.; Wang, J.; Sakakura, T.; Inagaki, Y.; Kakimoto, K.-I. Structural Evolution of $Na_{0.5}K_{0.5}NbO_3$ at High Temperatures. **2010**, *183*(11), 2731–2738.

[27] Orayech, B.; Faik, A.; López, G. A.; Fabelo, O.; Igartua, J. M. Mode-Crystallography Analysis of the Crystal Structures and the Low- and High-Temperature Phase Transitions in $Na_{0.5}K_{0.5}NbO_3$. *J. Appl. Cryst.* **2015**, *48*(2), 318-333.

[28] Zhang, N.; Glazer, A. M.; Baker, D.; Thomas, P. A. Structures of $K_{0.05}Na_{0.95}NbO_3$ (50-300 K) and $K_{0.30}Na_{0.70}NbO_3$ (100-200 K). *Acta Crystallogr. B* **2009**, *65*(Pt 3), 291-299.

[29] Fu, J.; Zuo, R.; Qi, H.; Chan, T. Identifying the Local Defect Structure in $(Na_{0.5}K_{0.5})NbO_3$: 1 Mol.% CuO Lead-Free Ceramics by x-Ray Absorption Spectra. *Appl. Phys. Lett.* **2019**, *114*(9), 092904.

[30] Al-Barakaty, A.; Prosandeev, S.; Wang, D.; Dkhil, B.; Bellaiche, L. Finite-Temperature Properties of the relaxor $PbMg_{\frac{1}{3}}Nb_{\frac{2}{3}}O_3$from Atomistic Simulations. *Phys. Rev. B* **2015**, *91*(21), 214117.

[31] Prosandeev, S.; Wang, D.; Ren, W.; Íñiguez, J.; Bellaiche, L. Novel Nanoscale Twinned Phases in Perovskite Oxides. *Adv. Funct. Mater.* **2013**, *23*(2), 234–240.

[32] Akbarzadeh, A. R.; Prosandeev, S.; Walter, E. J.; Al-Barakaty, A.; Bellaiche, L. Finite-Temperature Properties of $Ba(Zr,Ti)O_3$ Relaxors from First Principles. *Phys. Rev. Lett.* **2012**, *108*(25), 257601.

[33] Nahas, Y.; Akbarzadeh, A.; Prokhorenko, S.; Prosandeev, S.; Walter, R.; Kornev, I.; Íñiguez, J.; Bellaiche, L. Microscopic Origins of the Large Piezoelectricity of Leadfree $(Ba,Ca)(Zr,Ti)O_3$. *Nat. Commun.* **2017**, *8*, 15944.

[34] Walizer, L.; Lisenkov, S.; Bellaiche, L. Finite-Temperature Properties of $(Ba,Sr)TiO_3$ Systems

from Atomistic Simulations. *Phys. Rev. B* **2006**, *73*(14), 144105.

[35] Kalyani, A. K.; Senyshyn, A.; Ranjan, R. Polymorphic Phase Boundaries and Enhanced Piezoelectric Response in Extended Composition Range in the Lead Free Ferroelectric $BaTi_{1x}Zr_xO_3$. *J. Appl. Phys.* **2013**, *114*(1), 014102.

[36] Schiemer, J. A.; Lascu, I.; Harrison, R. J.; Kumar, A.; Katiyar, R. S.; Sanchez, D. A.; Ortega, N.; Salazar Mejia, C.; Schnelle, W.; Shinohara, H.; Heap, A. J. F.; Nagaratnam, R.; Dutton, S. E.; Scott, J. F.; Carpenter, M. A. Elastic and Anelastic Relaxation Behaviour of Perovskite Multiferroics I: $PbZr_{0.53}Ti_{0.47}O_3$(PZT)–$PbFe_{0.5}Nb_{0.5}O_3$(PFN). *J. Mater. Sci.* **2016**, *51*(24), 10727–10760.

[37] Spivakov, A. A.; Zakharov, Y. N.; Ter-Oganessian, N. V.; Lutokhin, A. G.; Panchenko, E. M.; Sakhnenko, V. P. Interrelation of Ferroelectricity and Tilting in Perovskites Using the Phase Transitions in $PbZr_{1x}Ti_xO_3$ as an Example. *Solid State Sci.* **2015**, *40*, 105–110.

[38] George, A. M.; Íñiguez, J.; Bellaiche, L. Optical Phonons Associated with the Low-Temperature Ferroelectric Properties of Perovskite Solid Solutions. *Phys. Rev. B* **2002**, *65*, 180301.

[39] Diéguez, O.; Aguado-Puente, P.; Junquera, J.; Íñiguez, J. Domain Walls in a Perovskite Oxide with Two Primary Structural Order Parameters: First-Principles Study of $BiFeO_3$. *Phys. Rev. B* **2013**, *87*(2), 024102.

[40] Wang, Y.; Nelson, C.; Melville, A.; Winchester, B.; Shang, S.; Liu, Z.-K.; Schlom, D. G.; Pan, X.; Chen, L.-Q. $BiFeO_3$ Domain Wall Energies and Structures: A Combined Experimental and Density Functional theory+U Study. *Phys. Rev. Lett.* **2013**, *110*(26), 267601.

[41] Bellaiche, L.; Íñiguez, J. Universal Collaborative Couplings between Oxygen-Octahedral Rotations and Antiferroelectric Distortions in Perovskites. Phys. Rev. B Condens. Matter Mater. *Phys. Rev. B* **2013**, *88*(1), 014104.

[42] Buhot, J.; Toulouse, C.; Gallais, Y.; Sacuto, A.; de Sousa, R.; Wang, D.; Bellaiche, L.; Bibes, M.; Barthélémy, A.; Forget, A.; Colson, D.; Cazayous, M.; Measson, M.-A. Driving Spin Excitations by Hydrostatic Pressure in $BiFeO_3$. *Phys. Rev. Lett.* **2015**, *115*(26), 267204.

[43] Gu, R.; Xu, R.; Delodovici, F.; Carcan, B.; Khiari, M.; Vaudel, G.; Juvé, V.; Weber, M. C.; Poirier, A.; Nandi, P.; Xu, B.; Gusev, V. E.; Bellaiche, L.; Laulhé, C.; Jaouen, N.; Manuel, P.; Dkhil, B.; Paillard, C.; Yedra, L.; Bouyanfif, H.; Ruello, P. Superorders and Acoustic Modes Folding in $BiFeO_3/LaFeO_3$ Superlattices. *Appl. Phys. Rev.* **2024**, *11*, 041415.

[44] Xu, B.; Wang, D.; Íñiguez, J.; Bellaiche, L. Finite-Temperature Properties of Rare-Earth-

Substituted $BiFeO_3$ Multiferroic Solid Solutions. *Adv. Funct. Mater.* **2014**, *25*(4), 552–558.

[45] Xu, R.; Delodovici, F.; Dkhil, B.; Paillard, C. Oxygen Tilt Driven Polar Superorders in $BiFeO_3$-Based Superlattices. *Phys. Rev. B* **2024**, *109*(22), L220101.

[46] Dixon, C. A. L.; Lightfoot, P. Complex Octahedral Tilt Phases in the Ferroelectric Perovskite System $Li_xNa_{1-x}NbO_3$. *Phys. Rev. B* **2018**, *97*(22), 224105.

[47] Kong, J.; Liu, J.; Marlton, F.; Jørgensen, M. R. V.; Pramanick, A. Local Structural Mechanism for Phase Transition and Ferroelectric Polarization in the Mixed Oxide $K_{0.5}Na_{0.5}NbO_3$. *Phys. Rev. B* **2021**, *103*(18), 184104.

[48] Yu, Q.; Zhu, F.-Y.; Cheng, L.-Q.; Wang, K.; Li, J.-F. Determination of Crystallographic Orientation of Lead-Free Piezoelectric (K,Na)NbO_3 Epitaxial Thin Films Grown on $SrTiO_3$ (100) Surfaces. *Appl. Phys. Lett.* **2014**, *104*(10), 102902.

[49] Lv, X.; Zhu, J.; Xiao, D.; Zhang, X.-X.; Wu, J. Emerging New Phase Boundary in Potassium Sodium-Niobate Based Ceramics. *Chem. Soc. Rev.* **2020**, *49*(3), 671–707.

[50] Zhang, N.; Zheng, T.; Wu, J. Lead-Free (K,Na)NbO_3-Based Materials: Preparation Techniques and Piezoelectricity. *ACS Omega* **2020**, *5*(7), 3099–3107.

[51] Zhang, M.-H.; Wang, K.; Du, Y.-J.; Dai, G.; Sun, W.; Li, G.; Hu, D.; Thong, H. C.; Zhao, C.; Xi, X.-Q.; Yue, Z.-X.; Li, J.-F. High and Temperature-Insensitive Piezoelectric Strain in Alkali Niobate Lead-Free Perovskite. *J. Am. Chem. Soc.* **2017**, *139*(10), 3889–3895.

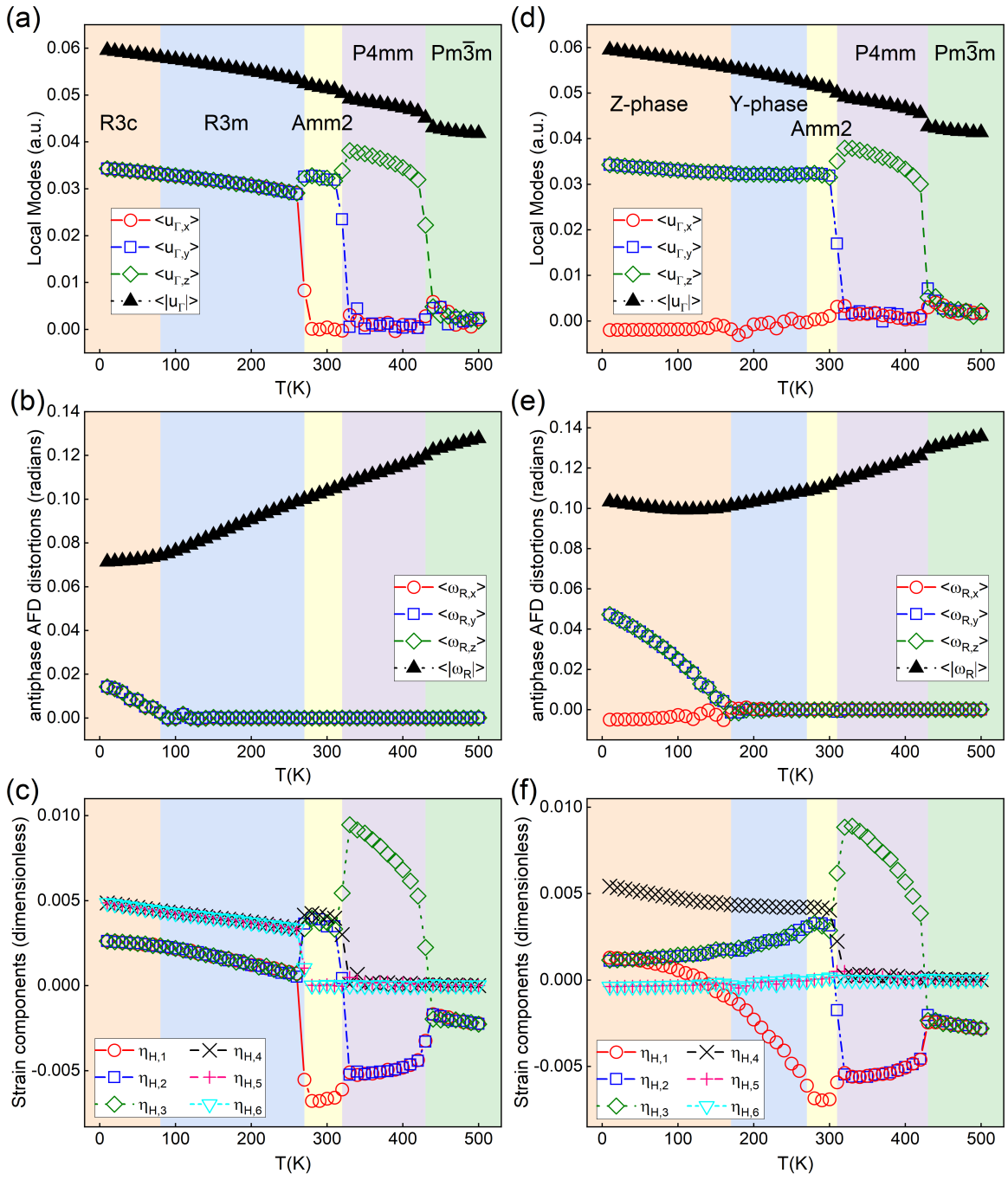

Figure 1. Properties of KNN-50 and KNN-43. Temperature dependency of (a) the Cartesian components of the $< \mathbf{u_\Gamma} >$ supercell average of the local mode vectors and of the $< |\mathbf{u_\Gamma}| >$ measure of the local magnitude of these local mode vectors ; (b) of the Cartesian components of the $< \omega_\mathbf{R} >$ antiphase tilting vector and the strength $< |\omega_\mathbf{R}| >$ of the AFD local distortions; and (c) of the six components of the homogeneous strain tensor for KNN-50, as predicted by the effective Hamiltonian of Eqs (1) and (2). Panels (d), (e) and (f) present similar data than panels (a), (b) and (c), respectively, but for KNN-43.

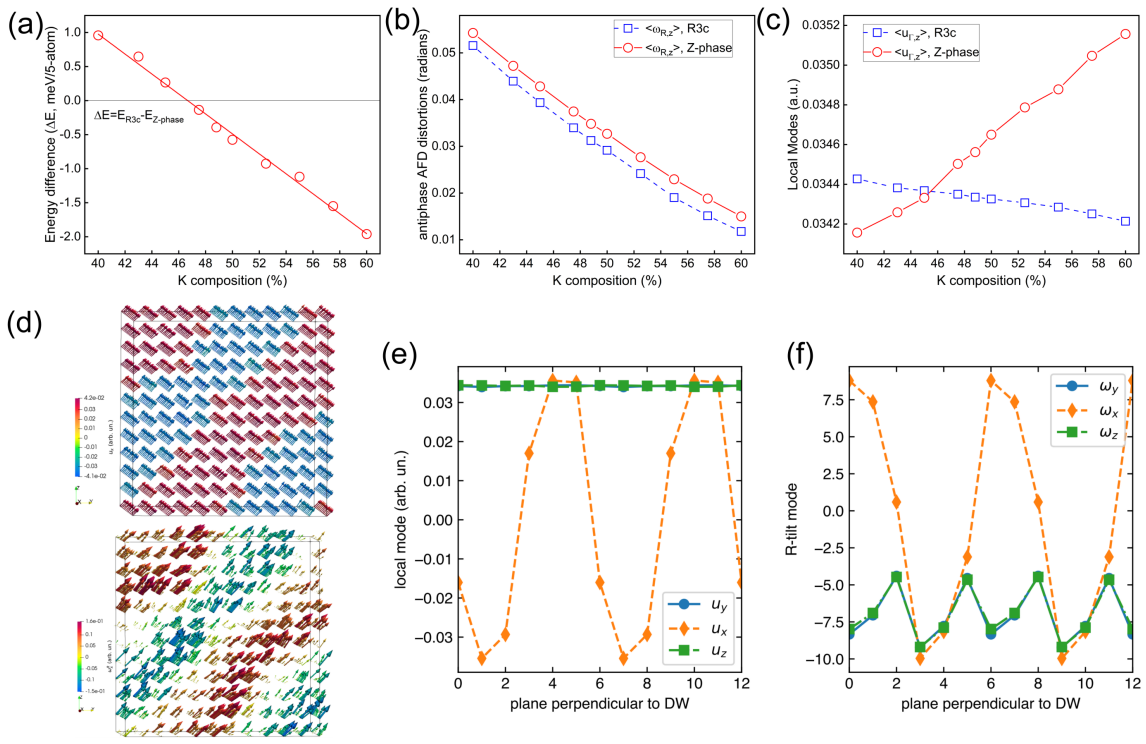

Figure 2. Comparison between the R3c and Z phases of KNN at 10K, as a function of K compositions, and characteristics of the Z-phase. Panel (a) represents the difference in internal energy between these two phases, with positive (respectively, negative) values indicating that the Z-phase (respectively, R3c state) is more stable. Panel (b) depicts the compositional behavior of the Cartesian components of the supercell average of the local mode vectors $< u_{\Gamma,z} >=< u_{\Gamma,y} >=< u_{\Gamma,x} >$ in the R3c phase, as well as $< u_{\Gamma,z} >=< u_{\Gamma,y} >$ in the Z phase (note the small range of the vertical scale). Panel (c) displays the compositional dependency of the Cartesian components of the antiphase tilting vector $< \omega_{R,z} >=< \omega_{R,y} >=< \omega_{R,x} >$ in the R3c state, as well as $< \omega_{R,z} >=< \omega_{R,y} >$ in the Z phase. Panel (d) displays a snapshot of the pattern of the local modes (up side) and of the $\omega_i(-1)^{n_x(i)+n_y(i)+n_z(i)}$ local antiphase tilting vectors (down side) in the Z phase at 10K. Panel (e) and (f) report the line profile of the local modes and antiphase tilting vectors along the $[0\bar{1}1]$ direction, respectively.

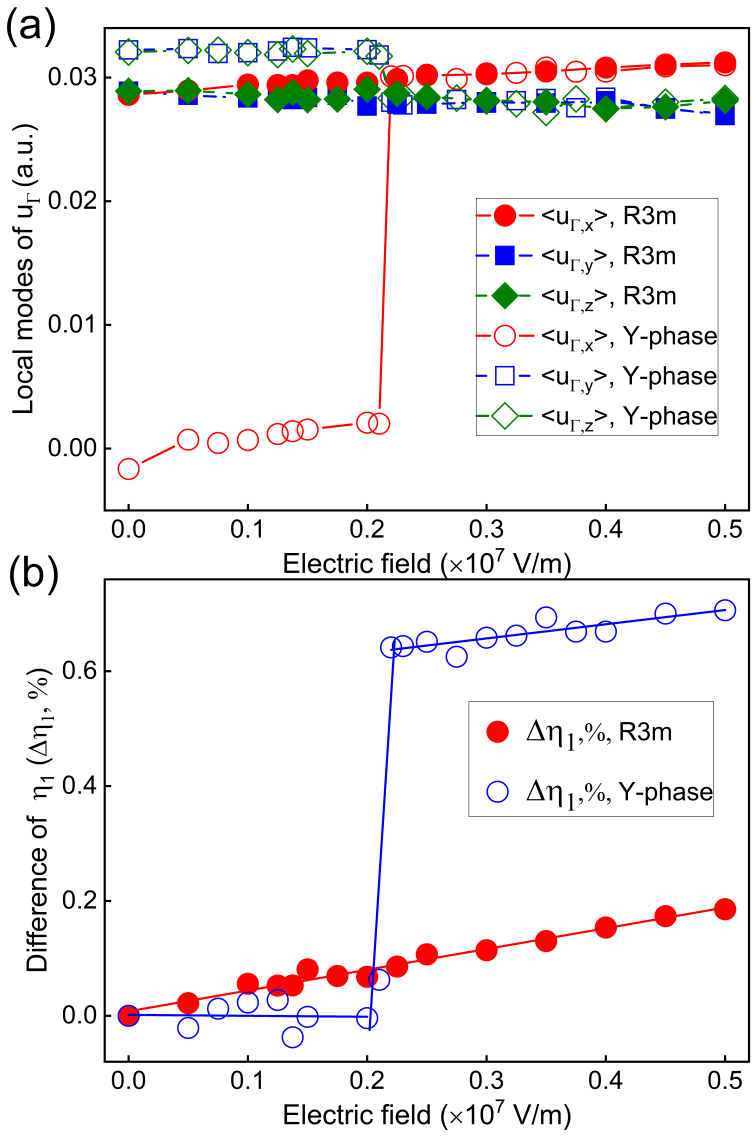

Figure 3. Properties of the Y and R3m phases of KNN-43 under an electric field applied along the x-direction at 260K. Panel (a) displays the Cartesian components of the $< \mathbf{u_\Gamma} >$ supercell average of the local mode vectors while Panel (b) shows the difference of the longitudinal component of the strain along the applied field's direction with respect to its zero-field value.

Table of Contents